Research Square

Preprints are preliminary reports that have not undergone peer review.
They should not be considered conclusive, used to inform clinical practice,
or referenced by the media as validated information.

Multi-analytical investigation of Eastern Han gilded copper coffin ornaments excavated from Wushan, Chongqing, China

Qiao Huang
Chongqing Normal University
YU Liu
Bazhong Cultural Relics Conservation and Research Center (Bazhong Grottoes Research Institute)
Heping Mao
Wushan Museum
Cunchong Sun
Chongqing China Three Gorges Museum
Xiaopan Fan
fxiaopan@163.com

Chongqing Normal University

Article

Keywords:

Posted Date: May 12th, 2026

DOI: https://doi.org/10.21203/rs.3.rs-9560836/v1

License: This work is licensed under a Creative Commons Attribution 4.0 International License.
Read Full License

Additional Declarations: No competing interests reported.

Version of Record: A version of this preprint was published at npj Heritage Science on September 5th, 2026. See the published version at https://doi.org/10.1038/s40494-026-02968-9.

Abstract

Six Eastern Han Dynasty gilded copper coffin ornaments excavated from Wushan, Chongqing, were analysed by optical microscopy, SEM-EDS, and Raman spectroscopy. Results reveal all samples were gilded with mercury amalgam and gilded layer thicknesses ranged from 0.3 to 8.0 μm. Two distinct gilding techniques were identified: gold-mercury amalgam gilding and gold-silver amalgam gilding. The gold-silver technique was associated exclusively with tombs containing silver funerary objects. The substrates consisted of red copper, low-lead bronze, and leaded tin bronze. Seven corrosion products were characterized, including malachite, cuprite, atacamite, azurite, cerussite, brochantite, and libethenite. Corrosion behavior was closely linked to the integrity of the gold layer, with corrosion notably intensified in the vicinity of engraved surface marks.

Introduction

Mercury gilding, also known as fire gilding or amalgam gilding [1], refers to a metal surface decoration technique widely used in ancient China. This technique developed during the Warring States Period (475 – 221 BC), and became increasingly sophisticated by the Han Dynasty (202 BC-220 AD) [2, 3]. Numerous gilded copper artifacts dating from the Han Dynasty have been unearthed. Among these finds, gilded coffin ornaments are particularly numerous in Chongqing, where they constitute a representative type of gilded copper artifacts, with the largest quantity and widest variety recovered in Wushan [4]. With the excavation of numerous gilded copper artifacts, studies have been conducted from a multi-faceted perspective, encompassing gilding techniques, corrosion mechanisms, and conservation strategies. These studies have laid a valuable foundation for the systematic investigation of such materials.

The mercury gilding technique employed on these artifacts has been investigated through microscopic observation, compositional analysis, and simulation experiments. These methods have focused on the microscopic morphology, structural characteristics, and elemental distribution on the surfaces of gilded copper artifacts [5–7]. Studies have identified two key features for recognizing mercury gilding: the presence of mercury in the gilded layer and the porous granular structure resulting from heat treatment [8, 9]. Gold and silver are generally distributed homogeneously within the gilded layer [10]. To ensure the quality of the gilded layer, ancient craftsmen tended to select pure copper substrates for gilding. This choice helped them avoid the negative effects of elements such as lead and zinc on the gilding outcome [11]. The gilding or silver-gilding techniques identified to date include three main methods: direct application of gold or silver amalgam, a composite technique that applies gold gilding first followed by silver gilding, and the use of a gold-silver alloy amalgam for silvering [12–14]. Simulation experiments have further confirmed that the number of gilding applications and the burnishing directly influence both the thickness and the density of the gilded layer [15].

The corrosion of gilded copper artifacts is influenced by multiple factors, including the burial environment, the gilded layer, and the copper substrate [16–18]. Elements such as chlorine (Cl), sulfur (S), and phosphorus (P) in the soil, together with variations in temperature and humidity, constitute the

main factors influencing corrosion [19–21]. The deterioration of gilded copper is mainly caused by galvanic coupling between copper substrate and gold, with surface corrosion products originating primarily from the migration of copper ions [22, 23]. Although an intact and compact gilded layer provides a degree of protection to the underlying copper substrate [24], a damaged one accelerates the corrosion of Cu, Sn, and Pb, each displaying distinct behaviors: Cu is extensively released; Sn is deposited as stable tin oxide (SnO_2); and Pb is partially present on the surface as lead carbonate ($PbCO_3$) [25, 26]. Studies in China have commonly reported corrosion products on gilded copper artifacts, including copper-bearing minerals such as cuprite, malachite, and azurite, as well as lead and tin corrosion products, such as cerussite and cassiterite. Notably, copper hydroxychlorides have appeared frequently in regions such as Xinjiang, Gansu, Jilin, Hebei, and Tianjin [27–30], but they remain relatively rare in southern China [31–34].

Wushan County in Chongqing, China (31°4'38.8"N, 109°52'31.4"E) lies on the north bank of the Yangtze River at the confluence with the Daning River (Fig. 1), where it experiences a humid subtropical monsoon climate with abundant rainfall. A wealth of gilded copper coffin ornaments in various shapes from the Han Dynasty was found in this area, including circular, cicada-shaped, human-shaped, Scarlet Bird-shaped, and Black Warrior-shaped forms [35]. These artifacts provide valuable material for understanding the social and cultural context of the Three Gorges region during the Han Dynasty, as well as for studying gilding techniques and artifact conservation. Previous research on the coffin ornaments from Wushan has focused primarily on typology and traditional manufacturing techniques, while investigations into gilding technology and corrosion mechanisms remain limited [13, 32, 36–38].

Six samples of gilded copper coffin ornaments from the Eastern Han Dynasty were selected from several burial sites, including Maituo Cemetery (M47, two samples), Longmenkou Cemetery (M23), Daxi Cemetery (M18), Shangxiping Cemetery (M5), and Shennvmiao Site (M23) (Fig. 1b). With the exception of Shennvmiao Site M23, which is an earthen cave tomb, all tombs are brick-chamber tombs. These sites are located along the Yangtze River, where most tombs have been poorly preserved due to river erosion and human activities. Skeletal remains and coffins are rarely preserved in these tombs, having been identified only in Longmenkou Cemetery M23. Besides the coffin ornaments, funerary artifacts were unearthed from Maituo Cemetery M47, including gold, silver, copper, and lacquerware, as well as glazed pottery, pottery figurines, and pottery architectural models. This tomb represents a relatively high-status burial [39]. Silver artifacts were also excavated from Longmenkou Cemetery M23. Except for Daxi Cemetery M18, where only a small number of copper coins, copper ornaments, and pottery were unearthed, copper artifacts were found in all other cemeteries, along with glazed pottery and pottery figurines [40]. Ultra-depth-of-field 3D video microscopy, SEM-EDS, and confocal Raman spectroscopy were employed to analyze the morphology, composition, and structure of the selected specimens, and to further investigate the material composition, manufacturing techniques, and corrosion characteristics of gilded copper artifacts. The results will provide a scientific basis for the conservation of such objects in the Three Gorges region.

Methods

Materials

Six fragments of gilded copper coffin ornaments from the Eastern Han Dynasty (AD 25–220) that had naturally detached and could not be restored to their original contexts were selected for analysis. Detailed information on the samples is presented in Table 1. The excavated coffin ornaments are generally heavily corroded, with their surfaces covered by corrosion products of various colors. Some also show signs of damage, including losses and cracks.

Table 1
The information of samples

Sample number	Archaeological number	Name	Date	Excavation Site
L1	1999WMM47:101	Black Warrior-shaped gilded copper coffin ornament	Eastern Han	Maituo Cemetery
L2	1999WMM47:102	Crescent-shaped gilded copper ear cup buckle	Eastern Han	Maituo Cemetery
L3	2003WLIM23:76	Gate attendant gilded copper coffin ornament	Eastern Han	Longmenkou Cemetery
L4	2013WDM18:4	Dragon-head huang-shaped gilded copper coffin ornament	Eastern Han	Daxi Cemetery
L5	2004WSM23:12	Scarlet Bird-shaped gilded copper coffin ornament	Eastern Han	Shennvmiao Site
L6	2002WS□M5:5	Scarlet Bird-shaped gilded copper coffin ornament	Eastern Han	Shangxiping Cemetery

Sample preparation

Before the experiment, the sample surfaces were gently cleaned with deionized water to minimize the impact of soil, dust, and other contaminants. The samples were then embedded in epoxy resin (the ratio of epoxy slow resin and hardener was 3:1) at room temperature, sequentially ground with silicon carbide sandpaper from 600 to 4000 grit, polished, rinsed with absolute ethanol, dried, and stored in sealed containers.

Microscopic analysis

A three-dimensional stereo digital microscope (VHX-5000, Keyence Ltd., Japan) equipped with a super-depth field zoom lens (VH-Z20W) was used to observe the corrosion products on the surfaces of the

samples and the rust layers on the cross-sections at magnifications of 20–200×.

Raman spectroscopy analysis

A Renishaw inVia Raman microscope system equipped with a 532 nm laser and a 50× objective lens was used to record the Raman spectra of the samples at room temperature. The spot size was 1 μm, and the spectra were collected over the range of 50-4000 cm^{-1}.

SEM-EDS analysis

Morphological observation and elemental analysis were performed using an FEI Quattro S field emission environmental scanning electron microscope (ESEM) equipped with an EDAX energy-dispersive spectrometer (EDS). Samples were analysed at a working distance of 10–12 mm, with a continuously adjustable magnification ranging from 10× to 1,000,000×. The accelerating voltage was set to 20 kV, and the chamber was maintained under high vacuum mode at 6×10^{-4} Pa. The energy resolution of the EDS system was better than 130 eV. The distribution and chemical composition of elements within individual phases were determined through a combination of point and mapping scan modes.

The micromorphology of the gilded layer was observed and the major elemental composition was determined using a desktop scanning electron microscope (TM4000PlusII, Hitachi Ltd., Japan) equipped with an AztecOne energy-dispersive spectrometer (Oxford Ltd., UK), operating in standard vacuum mode. Samples were analysed at a working distance of 10 mm with an accelerating voltage of 20 kV, and images were acquired in backscattered electron (BSE) mode. All data results are reported to one decimal place.

Results

Microscopy results

Micrographs of the samples (Fig. 2) show that the corrosion products on the ungilded surface are predominantly green, intermixed with brown, reddish-brown, blue, and white corrosion products. Irregular patch-like or layered accumulations formed on the surface of L4 (Fig. 2d). The corrosion products were loosely structured and present mostly as powders or granules.

Cross-sectional micrographs (Fig. 3) show that the ungilded surface of each sample exhibited a double-layer structure consisting of an inner brown corrosion layer and an outer green corrosion layer, though the thickness of each layer varied across samples. The extent of corrosion products on the gilded surface varied across samples. Localized accumulations were present on L1, while fewer corrosion products were observed on L3 and L5, and distinct corrosion layers were observed on L2, L4, and L6. Localized corrosion zones formed at cracks in the gold layer of L2, with corrosion extending from the gold layer into the interior of the substrate. By contrast, in the other samples, corrosion advanced from

the ungilded surface into the substrate. Among them, the corrosion in L3, L4, and L6 had extended to the central region of the substrate.

On the gilded surface of L1 (Fig. 3a), two regularly shaped "small triangular" marks with continuous edges were visible. Their morphological features were similar to the "∨"-shaped sharp tool engraving marks reported in the literature [33, 41]. Similarly, a comparable "small triangular" mark was observed on the gilded surface of L2 (Fig. 3b). Corrosion was notably intensified in the vicinity of such marks. L1 and L2 were both unearthed from M47 at the Maituo cemetery and shared similar technological and manufacturing characteristics.

Raman spectroscopy results

Corrosion products of different colors were characterized by Raman spectroscopy. The results are presented in Fig. 4 and Table 2. The Raman peaks of the green corrosion product at 181, 273, 436, 538, 1092, 1493, and 3379 cm^{-1} (Fig. 4a) were ascribed to malachite by comparison with the Raman spectrum of malachite ($Cu_2(CO_3)(OH)_2$) [42]. Raman peaks appeared at 218, 627, and 1053 (vs) cm^{-1} (Fig. 4b), which were consistent with those of cuprite (Cu_2O) [43] and cerussite ($PbCO_3$) [44], indicating the presence of a mixture of these two phases. The Raman peaks at 144, 393, 482, 602, 974 (vs), 1098, 3397, and 3590 cm^{-1} (Fig. 4c) correspond to the characteristic Raman peaks of brochantite ($Cu_4SO_4(OH)_6$) [45]. The Raman peaks of the blue granular corrosion products (Fig. 4d) are located at 141, 251, 401, 764, 1098, 1428, 1580, and 3432 cm^{-1}, which are consistent with the standard Raman spectrum of azurite ($Cu_3(CO_3)_2(OH)_2$) [43]. The Raman peaks of the light green corrosion product (Fig. 4e) at 141, 365, 513, 896, 971, 3357, and 3443 cm^{-1} correspond to the characteristic Raman peaks of atacamite ($Cu_2Cl(OH)_3$) [44]. The Raman peaks at 156, 197, 388, 484, 973, and 1077 cm^{-1} (Fig. 4f) match the characteristic peaks of libethenite ($Cu_2(OH)PO_4$) [46].

Table 2
Raman results of corrosion products.

Sample number	Archaeological number	Corrosion products
L1	1999WMM47:101	Malachite, cuprite, brochantite, cerussite
L2	1999WMM47:102	malachite, cuprite, azurite
L3	2003WLIM23:76	malachite, cuprite, atacamite
L4	2013WDM18:4	malachite, cuprite, libethenite
L5	2004WSM23:12	malachite, cuprite, atacamite, brochantite
L6	2002WS□M5:5	malachite, cuprite, libethenite, brochantite

SEM-EDS results

The cross-sections of the gilded layers were examined by SEM-EDS, and the thickness of the gilded layers was measured. The corresponding results are presented in Fig. 5 and Table 3, respectively.

The thickness of the gilded layers across the six samples ranged from 0.3 to 8.0 μm. The gilded layers of L2 and L4 were relatively thin and uneven, measuring 0.3–2.8 μm. In contrast, L3 and L6 exhibited comparatively thicker and more uniform gilded layers, with thicknesses ranging from 1.9 to 5.4 μm. In addition, a localized accumulation of gold was observed on L1 (Fig. 5a), with a thickness of approximately 8.0 μm, exceeding the measurements recorded elsewhere on the same piece. It is hypothesized that this accumulation resulted from the application of gold amalgam paste into surface grooves during manufacture [14].

Mercury (Hg) was detected in all the gilded layers, with contents ranging from approximately 3–16%, which is consistent with the characteristic technical feature of ancient mercury gilding. Furthermore, Cu, Au, and Ag were simultaneously identified. The Cu content ranged from 12% to 45%, originating primarily from the diffusion out of the copper substrate or the incorporation of corrosion products [47]. The concentrations of Au, Ag, and Hg were linked to the raw materials used to prepare the amalgam. In the gold layers of L1 and L3, the Au content was approximately 26–52% and the Ag content approximately 1–20%. The high Ag content suggested intentional addition, implying the use of a gold-silver amalgam [13]. In the remaining four specimens, the Au contents lay between approximately 48% and 75%, while Ag remained below 2%. The minor amounts of silver detected were likely due to impurities in the native gold, reflecting the level of gold refining technology at the time.

Table 3
Elemental analysis results of the cross-sections of the gilded layers.

Sample number	Thickness of the gilded layer	Elemental Components (wt%)			
		Cu	Ag	Au	Hg
L1	1.1-8.0 μm	34.2	13.7	34	15.8
		44.3	5.4	38.7	6.3
		15.4	1.8	68.2	10.0
L2	0.3–2.8 μm	35.3	0.8	59.5	4.0
		33.0	2.0	60.0	3.8
		42.2	< 0.5	52.3	4.5
L3	2.8–5.4 μm	15.7	19.3	45.6	15.9
		15.2	15.5	51.6	13.2
		12.1	18.0	50.5	15.7
L4	0.3–1.7 μm	32.4	1.3	58.9	5.3
		39.4	0.9	48.2	6.8
		36.0	1.9	55.3	5.0
L5	1.3–2.8 μm	17.3	1.2	71.6	9.1
		21.9	< 0.5	70.2	6.7
		16.3	< 0.5	74.7	8.4
L6	1.9–4.3 μm	31.1	< 0.5	63.7	3.6
		29.2	1.0	60.9	6.0
		31.2	0.6	63.1	4.7

The results of the SEM-EDS cross-sectional analysis are presented in Fig. 6–10 and Table 4–7. In the outer corroded area of L1, the Cu concentration was lower than that in the central part of the substrate. As shown in Fig. 6, areas 1 and 2 exhibited Cu contents of approximately 91–95%, Sn below 1%, and Pb ranging from approximately 2% to 4%. These locations consisted predominantly of copper corrosion phases, along with minor lead corrosion compounds. However, the Cu proportion in area 3 was 97.6%, with relatively low Sn and Pb, which was consistent with the presence of cuprite identified by Raman spectroscopy. Additionally, on the outer side of the gilded layer (areas 4 and 5), the Pb concentrations were notably elevated, reaching approximately 28–30%. This enrichment was attributed to the migration and deposition of Pb during the corrosion process, corresponding to the lead corrosion product cerussite detected by Raman analysis.

The elemental distribution maps in the vicinity of the "small triangular" engraving marks on L1 are shown in Fig. 7. During corrosion, Cu continuously migrated toward both surfaces of the substrate, forming copper corrosion phases on the gilded surface and the outer side of the substrate. A marked difference in Pb content was observed between the two sides of the gold layer, indicating that Pb migrated toward and was deposited on the gold layer surface during corrosion [48]. In the engraved areas, lead and copper corrosion products accumulated on the gold layer surface, forming a sandwich structure composed of cuprite-cerussite-cuprite (or malachite) layers.

Table 4
EDS results of L1.

Analysis area	**Elemental Components (wt%)**		
	Cu	**Sn**	**Pb**
1	93.8	0.8	2.4
2	91.9	1.0	3.8
3	97.6	0.5	0.6
4	66.8	1.3	30.1
5	68.8	0.8	28.4
6	94.3	0.8	3.1

The Cl contents in areas 1 and 3 were approximately 25–29%, substantially higher than those in other regions, while Cu contents ranged from about 67% to 73% (Table 5). In the corroded area on the ungilded side of the substrate, the Cl content was markedly elevated relative to that observed on the gilded surface. The results indicated that Cu migrated significantly from the substrate during the corrosion process, and the copper corrosion products formed on the ungilded side were attributed to the reaction of mobilized Cu with chloride ions. Combined with the Raman analysis, these areas were inferred to contain atacamite. In areas 2, 4, and 5, the Cu contents were markedly higher than those in other regions, whereas Sn and Pb contents remained low. These areas were therefore attributed to copper oxides, which were consistent with the presence of cuprite identified by Raman spectroscopy.

Table 5
EDS results of L3.

Analysis area	Elemental Components (wt%)			
	Cu	Sn	Pb	Cl
1	67.8	0.7	1.1	28.9
2	97.1	< 0.5	0.6	0.7
3	72.7	< 0.5	0.7	25.1
4	97.6	0.6	0.6	< 0.5
5	97.5	< 0.5	0.7	< 0.5

The elemental analysis results for L4 are presented in Table 6. Areas 1 and 2 exhibited relatively high Cu contents (approximately 97%) with low concentrations of other elements, corresponding to cuprite as detected by Raman analysis. Area 3 was located within a dark gray corroded region and exhibited a Cu content of approximately 94%, which was consistent with the presence of malachite identified by Raman spectroscopy. In areas 4 and 5, the P contents reached approximately 13% and the Cu contents were 75–78%, indicating the presence of phosphorus-bearing corrosion products; this was consistent with the libethenite identified by Raman spectroscopy. The P content in the corroded area on the ungilded side of L4 was markedly higher than that on the gilded surface.

Table 6
EDS results of L4.

Analysis area	Elemental Components (wt%)			
	Cu	Sn	Pb	P
1	97.1	0.7	0.8	< 0.5
2	97.4	0.5	0.7	< 0.5
3	93.9	0.9	1.1	2.3
4	77.5	1.2	2.1	13.6
5	75.8	1.2	1.7	12.8

In the dark areas within the substrate of L6 (areas 1, 2, 6, and 7), Cu contents of approximately 81–84% were detected, accompanied by Pb ranging from 2.7% to 4.3% and S at about 10–12%. These locations exhibited lower Cu and markedly higher S contents relative to other areas within the substrate. Raman analyses suggested the presence of brochantite in these regions. In the outermost areas (4 and 5), the Cu, Sn, and Pb contents differed substantially from those in the substrate, with measurements of 69–76%, 5–13%, and 2–6%, respectively. These variations were attributed to element migration during the corrosion process.

Table 7
EDS results of L6

Analysis area	Elemental Components (wt%)			
	Cu	Sn	Pb	S
1	81.8	0.9	4.3	11.6
2	92.9	0.7	2.7	2.1
3	97.6	0.5	0.5	< 0.5
4	75.4	5.9	3.2	< 0.5
5	69.6	12.9	5.5	< 0.5
6	83.2	0.8	3.9	10.7
7	83.4	0.7	4.3	10.1

Among copper, tin, and lead, the last is the most reactive and therefore tends to corrode first and become depleted, whereas tin corrodes most slowly and tends to remain where it formed [25]. Based on the corrosion products identified above and the SEM-EDS results, the substrate of L1 exhibited a low lead content in the analysed areas, except those rich in lead-bearing corrosion phases. Combined with the elemental mapping results (Fig. 11), L1 was inferred to be a low-lead bronze. Similarly, a gilt-bronze belt ornament unearthed in the Ili region of Xinjiang, reported to contain approximately 2% lead, has been identified as a low-lead bronze [28]. By comparison, the substrate of L6 was identified as a leaded tin bronze, containing 2%-6% Pb and 6%-13% Sn, and is compositionally comparable to the substrates of gilt-bronze artifacts excavated from the Han tombs at Jiulong Mountain in Qufu, Shandong [48]. The remaining samples consisted of red copper. L5 contained over 99% Cu and was cast from nearly pure copper, whereas the other red copper samples had Cu contents of approximately 97.5%, showing only minor variation among them.

Discussion

The use of mercury and heat treatment distinguishes fire-gilding from other ancient plating techniques. In this process, a substantial portion of mercury escapes during heating, yet a certain amount remains in the gold layer as elemental mercury or an alloy [9, 49]. The presence of residual mercury thus serves as the most reliable indicator of the fire-gilding process [50, 51]. In the present study, mercury was detected in all the gilded layers at concentrations of approximately 3–16%, confirming the use of fire-gilding. Silver was also detected in the gilded layers of L1 and L3, indicating that a gold-silver amalgam was employed for these two artifacts [13, 14]. Both samples were unearthed from tombs containing silver funerary objects, whereas the remaining samples, with the exception of L2, were recovered from tombs in which no silver artifacts were found and were gilded with a gold-mercury amalgam. This suggests that the selection of the amalgam was closely linked to tomb rank and the presence of silver funerary objects.

Furthermore, although L1 (a disc-shaped ornament) and L2 (an ear cup fastener) were unearthed from the same cemetery, the amalgams used in their gilded layers were different, reflecting a conscious selection of techniques tailored to different types of artifacts. Within the gilded layer of L1, the silver content varied considerably, being lower in thicker regions and higher in thinner ones. This uneven distribution was likely attributable to the thin-walled form of the object and the grooves left by engraving, both of which led to a non-uniform application of the amalgam. Localized thickening or repair may also have resulted in this phenomenon [52].

The variation in gilded layer thickness is related to tomb rank and the functional characteristics of the funeral objects. According to the burial information, the two coffin ornaments corresponding to L3 and L4 measured approximately 0.05 cm in overall thickness and shareed similar forms (width approximately 2–4 cm, with a difference in length of about 10 cm) [39]. Nevertheless, the gilded layer on L3 measures approximately 2.8–5.4 μm, whereas that on L4 ranges from only 0.3 to 1.7 μm. The tomb from which L4 was recovered is of lower rank, lacking the gold or silver artifacts characteristic of higher-status burials. A thin gold layer was therefore deemed sufficient, likely aimed at economizing on production costs. In addition, the functional characteristics of the artifacts also influence gilded layer thickness. L1 and L2 were unearthed from the same tomb, yet their gilded layers differ in thickness. L1 is a disc-shaped coffin ornament, whereas L2 is a crescent-shaped copper ear cup fastener. The irregular surface and thin-walled form of L2 made gilding more difficult, and a thick gilded layer would also have resulted in unnecessary waste of gold. The thinner gilding on L2 therefore reflects a technical decision based on its form and intended function.

The gilded layers of the six coffin ornaments excavated from Han tombs in Wushan range in thickness from 0.3 to 8.0 μm. It has been reported that the thickness of gilded layers typically falls between 2 and 10 μm [53, 54]. A layer exceeding 10 μm increases the technical difficulty of gilding and leads to unnecessary waste of gold [55], whereas an excessively thin layer may appear reddish due to an elevated Cu content, compromising the desired visual effect. However, several studies have reported gilded layers thinner than 2 μm. For example, the thin gold layers on medieval gilded copper hollow pendants excavated from Prague Castle measure less than 2 μm in thickness [7]. The gilded silver-bronze artifacts unearthed from the tomb of the Marquis of Haihun exhibit gold layer thicknesses ranging from 1.5 to 7.24 μm [56], and the gilded red copper objects recovered from the Xiaoling mausoleum of Emperor Wu of the Northern Zhou Dynasty display gold layer thicknesses mainly concentrated between 1 and 5 μm [57]. Three gilded copper coffin ornaments previously unearthed in Chongqing have gilded layer thicknesses of approximately 1-2.5 μm [58]. In this study, the gilded layers of L2, L4, and L5 range in thickness from 0.3 to 2.8 μm, representing some of the thinner gilded layers reported to date. It is suggested that the production of such thin gilded layers is related to the thin-walled form of these coffin ornaments. These observations indicate that during the Eastern Han Dynasty, craftsmen were not only capable of adapting the gilding technique flexibly according to material properties and functional requirements, but could also apply a gold-silver amalgam directly to the copper surface without the need for an initial gold layer followed by silver gilding. This reflects a relatively mature level of gilding technology at the time.

The integrity of the gold layer and its surface finishing techniques have a significant influence on the corrosion of the copper coffin ornaments. Phosphorus and chlorine, both present in the burial environment, are detected at higher contents on the outer side of the non-gilded substrate but are found only in minor amounts on the surface of the gilded layer. This indicates that an intact gold layer effectively protects the copper substrate and retards the corrosion process. Under such conditions, corrosion tends to propagate gradually from the outer side of the substrate toward its interior. Conversely, a damaged gold layer may accelerate localized corrosion, allowing it to extend from the compromised area into the substrate. In the vicinity of the "small triangular" engraving marks observed on the gilded surfaces of L1 and L2, corrosion is notably intensified, indicating that microstructural alterations introduced by mechanical working accelerate localized attack [59, 60]. A damaged gilded layer provides pathways for ion migration, which not only promotes the dissolution of the copper substrate and the transport of corrosion products but also facilitates the ingress of water, oxygen, and soil constituents from the burial environment [61]. The manual operations involved in the gilding process are inherently variable. Differences in engraving force, uneven application of the gold amalgam, and insufficient subsequent polishing can all create localized weaknesses in the gold layer, which may subsequently develop into cracks or discontinuities. In the burial environment, such areas are prone to evolve into localized corrosion zones [62]. The progressive accumulation of corrosion products further weakens the adhesion between the gilded layer and the substrate, leading to lifting and spalling of the gold layer and ultimately compromising the integrity and state of preservation of the artifacts.

The corrosion products identified on the gilded copper coffin ornaments from Wushan include malachite, cuprite, atacamite, azurite, cerussite, brochantite, and libethenite. Among these, cuprite and malachite are distributed on both sides of the substrate, whereas cerussite is largely concentrated on the gilded side. Brochantite and atacamite accumulate around heavily corroded cavities and along the outer side of the substrate. Corrosion products previously identified in the Chongqing region include cuprite, cerussite, malachite, atacamite and azurite [13, 31, 32], while brochantite and libethenite were additionally detected in the Wushan area. The corrosion products are dominated by copper compounds, with only minor amounts of lead-bearing corrosion phases, a feature attributable to the substrate composition. L1 and L6 were identified as a low-lead bronze and a leaded tin bronze respectively, based on the EDS and Raman results. The remaining samples are all of red copper, consistent with the substrate material of gilded copper coffin ornaments previously reported in Chongqing [13, 32]. In the red copper substrates, copper continuously migrates toward both sides of the substrate, first forming cuprite on the gilded surface and on the outer side of the substrate, and subsequently transforming into secondary corrosion products such as malachite and azurite in the presence of CO_2 and H_2O. In the leaded bronze substrate, lead migrates preferentially toward the gilded surface during corrosion and is deposited as cerussite. This phenomenon is particularly pronounced in the engraved areas, where lead and copper corrosion products accumulate on the gold layer surface, forming a sandwich structure consisting of cuprite-cerussite-cuprite (or malachite) layers.

Wushan is situated at the confluence of the Yangtze River and the Daning River, an area historically prone to flooding [63]. The soils of the Three Gorges region are well-drained yet possess a certain water-

retention capacity, characteristics that enhance their corrosivity [64]. The abundant moisture and the presence of ions such as SO_4^{2-}, CO_3^{2-}, Cl^-, and HCO_3^- in the soil provide favorable conditions for the formation of corrosion products including malachite, atacamite, azurite, and brochantite [65]. The phosphorus detected in the corrosion products likely originated from hydroxyapatite ($Ca_5(PO_4)_3OH$), the principal inorganic constituent of human bones and teeth in the tombs. The formation of phosphate corrosion products may be connected with the particular burial environment of the Three Gorges area, a relationship further supported by the detection of similar phosphates on bronze artifacts from several sites located along the Yangtze River or its tributaries [66].

Abbreviations

SEM
Scanning electron microscope
EDS
Energy dispersive spectrometer.

Declarations

Competing interests

The authors declare no competing financial interests.

Author Contribution

Q.H.: methodology, investigation, data curation, visualization, writing—original draft. Y.L.: investigation, experimental assistance. H.M.: sample information and background, writing—review and editing. C.S.: Raman experimental assistance, resources, writing—review and editing. X.F.: methodology, formal analysis, project administration, supervision, writing—review and editing. All authors read and approved the final manuscript.

Acknowledgement

This research was supported by the Chongqing Municipal Administration of Cultural Heritage through the Project “Study on the Corrosion Mechanisms of Bronze Artifacts Unearthed from the Three Gorges Area”. The authors would like to thank the Wushan Museum for supplying the samples. We also greatly thank the Chongqing China Three Gorges Museum for providing the experimental instruments.

Data Availability

All data generated or analysed during this study are included in this published article and its supplementary information files.

References

1. Laskaris N, Varalis I, Tsodoulos C, et al. Evidence of Au-Hg gilding process in post byzantine ecclesiastical silverwares (Chalices) of eastern Thessaly by PXRF. Mediterranean Archaeol Archaeometry. 2020;20:189–203.
2. Mou Y. Brief report on excavation of Tomb 306 of the Warring States period in Shaoxing. Cult Relics. 1984;01:10–26. (in Chinese).
3. Gao X. A Preliminary Study on Gilded Wares of Warring States Period and Related Issues. J Natl Museum China. 2012;04:43–55. (in Chinese).
4. Xiao B, Chen R, Yang X. A Review of the Funeral Gilt-Copper Coffin Ornaments of the Han and Six Dynasties'Tombs in Three-Gorge Region. J Natl Museum China. 2024;02:119–40. (in Chinese).
5. Masi G, Chiavari C, Avila J, et al. Corrosion investigation of fire-gilded bronze involving high surface resolution spectroscopic imaging. Appl Surf Sci. 2016;366:317–27.
6. Ingo G, Guida G, Angelini E, et al. Ancient mercury-based plating methods: combined use of surface analytical techniques for the study of manufacturing process and degradation phenomena. Acc Chem Res. 2013;46:2365–75.
7. Ottenwelter E, Barčáková L, Josse C, et al. Technological characterisation of early Medieval gilded copper hollow pendants (gombiky), from Mikulčice (Moravia) and Prague Castle (Bohemia). Archaeol Anthropol Sci. 2020;12:1–22.
8. Cesareon R. Gold gildings, and tumbaga from the Moche tomb of the Lady of Cao: an EDXRF test for the internal ratio method. X-Ray Spectrom. 2019;48:202–7.
9. Kobiela T, Nowakowski B, Duś R. The influence of gas phase composition on the process of Au-Hg amalgam formation. Appl Surf Sci. 2003;206:78–89.
10. Figueiredo E, Silva RJC, Araújo MF, et al. Identification of ancient gilding technology and Late Bronze Age metallurgy by EDXRF, Micro-EDXRF, SEM-EDS and metallographic techniques. Microchim Acta. 2010;168:283–91.
11. Borges R, Tissot I, Seruya AI et al. Gilding and silvering surface decoration techniques, and copper provenance studies of the tomb of D. Afonso of Portugal (15th century). *X-Ray Spectrometry.* 37, 338–345 (2008).
12. Susan La Niece. Silvering. Susan La Niece and Paul Craddock eds. Metal Plating and Patination: Cultural, Technical and Historical Developments. Oxford: Butterworth Heinemann; 1993.
13. Yang X, Zhou h. Yi, j. Primary study on gold gilt and silver gilt copper wares excavated from Wushan county in Chongqing City. Jianghan Archaeol. 2013;03:131–4. (in Chinese).
14. Yang W, Zhang H, et al. A Comparative Study on Three Gilding Danglu Crafts Unearthed from the Outer Coffin of Haihun Marquis in the Western Han Dynasty. Cult Relics South China. 2022;02:115–

24. (in Chinese).
15. Cai Y, Hu D. Research on Golding Technology. *A Collection of Studies on Archaeology*. 00, 59–75 (2020) (in Chinese).
16. Scott DA. Copper and Bronze in Art: Corrosion, Colorants, Conservation. Malibou, USA: The J. Paul Getty Conservation Institute; 2002.
17. Tylecote RF. The effect of soil conditions on the long-term corrosion of buried tin-bronzes and copper. J Archaeol Sci. 1979;6:345–68.
18. Squarcialupi MC, Bernardini GP, Faso V, et al. Characterisation by XPS of the corrosion patina formed on bronze surfaces. J Cult Herit. 2002;3:199–204.
19. Ingo GM, Riccucci C, Lavorgna M, et al. Surface investigation of naturally corroded gilded copper-based objects. Appl Surf Sci. 2016;387:244–51.
20. Singh V, Singh S. A study on environmental corrosion of gilded heritage structures of Royal Palace Patan. Nepal Indian J Pure & Appl Physics. 2017;55:890–5.
21. Alviz-Meza A, Rodríguez-Reyes JCF, Chacaliaza JA. Thermodynamic stability of gilded copper and pigments at high relative humidity and at environmental conditions of Lima, Perú. *Journal of Physics: Conference Series*. 1938, 6 (2021).
22. Ingo GM, Riccucci C, Pascucci M, et al. Combined use of FE-SEM + EDS, ToF-SIMS, XPS, XRD and OM for the study of ancient gilded artefacts. Appl Surf Sci. 2018;446:168–76.
23. Yu X, Liang C, Li W, et al. IBE-XPS investigation of the gilded layer from the Eastern Han Dynasty naturally corroded gilt-bronze. npj Herit Sci. 2025;13:257.
24. Chiavari C, Bernardi E, Balbo A, et al. Atmospheric corrosion of fire-gilded bronze: corrosion and corrosion protection during accelerated ageing tests. Corros Sci. 2015;100:435–47.
25. Wang J, Xu C, Lv G. Chemical behavior of mass transfer at the bronze/environment interface. Chin J Mater Res. 2004;3:244–50. (in Chinese).
26. Cai Y, Hu D, Guan L, et al. A Study on the Migration and Change of Gold Plated Bronze Danglu Copper and Tin Elements Unearthed in Chariot Pit Wares of the Tomb of Liu He, Marquis Haihun. Cult Relics South China. 2020;06:180–8. (in Chinese).
27. Song J, Guan M, Liu H et al. Corrosion and Protection of a Begonia Style Hand Stove of Enamel Flowers and Consecration of Birds and Animals. *Corrosion & Protection*. 44, 36–41 (2023) (in Chinese).
28. Zhu S, Liu C, Zhu Y. The Scientific Analysis and Preservation of the Gilt Bronze Belt Fittings Unearthed in Ili, Xinjiang. Relics Museology. 2019;05:101–7. (in Chinese).
29. Gao X, Zhao X, Wang Z, et al. Examination and analysis of gilded artifacts excavated from tomb 1041 at Yushan, Ji'an. North Cult Relics. 2011;02:99–103. (in Chinese).
30. Lü L. Research on conservation of the early Six Dynasties gilt bronze animal head appliqué. Sci Conserv Archaeol. 2010;22:76–80. (in Chinese).

31. Yang X, Liu P, Ye L, et al. Using hydrogels to remove rust from gilt bronzes in the Chongqing area. Sci Conserv Archaeol. 2019;31:35–40. (in Chinese).
32. Jin P, Yang X, Li N, et al. Survey on the Corrosion of Fire-Gilded Copper Fragments from Wushan District in Chongqing. Corros Prot. 2025;46:9–15. (in Chinese).
33. Ji J, Ma L, Bai K, et al. Analysis of Bajunshoucheng gilding bronze seal of the Eastern Han dynasty in Guizhou by scanning electron microscope. J Chin Electron Microscopy Soc. 2019;38:43–7. (in Chinese).
34. Song J, Gao F, Liu H, et al. Scientific Analysis of the Boshan Furnace from the Tomb of the Haihun Marquis. Archaeol Cult Relics. 2025;06:124–8. (in Chinese).
35. The Chongqing Municipal Administration of Cultural. Chongqing Reservoir Area Archaeological Report Collection 1998 Volume. Sci Press (2003) (in Chinese).
36. Cong D, Luo Z. Discovery and research on the Eastern Han Dynasty gilt-bronze plaque ornaments from Wushan County. Chongqing Archaeology. 1998;12:77–86. (in Chinese).
37. Su K. Images and Belief of the Bi-Shaped Gold and Silver Plated Bronze Coffin Ornaments from the Eastern Han Dynasty. Sichuan Cult Relics. 2021;05:48–71. (in Chinese).
38. Xiao B, Yang X, Zou H, et al. Study on gilt-bronze artifacts unearthed from the Xiajiang region, Chongqing, dating from the Warring States to the Six Dynasties period. South Ethnology Archaeol. 2015;00:129–59. (in Chinese).
39. The Chongqing Municipal Administration of Cultural & The Chongqing Migration Bureau. Maituo Cemet Wushan Cty Science Press. (2018) (in Chinese).
40. The Chongqing Municipal Administration of Cultural. Chongqing Reservoir Area Archaeological Report Collection 2003 Volume. Science Press. (2019) (in Chinese).
41. Yang J, Wei Q, Zhang Z, et al. Scientific research on gold-decoration techniques of Warring States bronze chime bells in Sichuan Museum. Sci Conserv Archaeol. 2022;34:69–80. (in Chinese).
42. Bouchard M, Smith DC. Catalogue of 45 reference Raman spectra of minerals concerning research in art history or archaeology, especially on corroded metals and coloured glass. Spectrochimica Acta Part A. 2003;59:2247–66.
43. Ivanda M, Waasmaier D, Endriss A, et al. Low-temperature anomalies of cuprite observed by Raman spectroscopy and X-ray powder diffraction. J Raman Spectrosc. 1997;28:487.
44. Edwards HGM, Chalmers JM. Raman Spectroscopy in Archaeology and Art History, edited by H.G.M. Edwards and J.M. Chalmers. *The Royal Society of Chemistry.* (2005).
45. Hayez V, Guillaume J, Hubin A, et al. Micro-Raman spectroscopy for the study of corrosion products on copper alloys: setting up of a reference database and studying works of art. J Raman Spectrosc. 2004;35:732–8.
46. Kharbish S, et al. Raman spectra of oriented and non-oriented Cu hydroxy-phosphate minerals: Libethenite, cornetite, pseudomalachite, reichenbachite and ludjibaite. Spectrochim Acta Part A Mol Biomol Spectrosc. 2014;130:152–63.

47. Kantarelou V, Karydas AG, Sokaras D, et al. In-situ scanning micro-XRF analyses of gilded bronze figurines at the National Museum of Damascus. J Anal At Spectrom. 2015;30:1787–98.
48. MA R, XU H, NING H, et al. Corrosion characteristics of fire-gilded bronzes excavated from the Jiulongshan Han tomb in Qufu,Shandong Province. J Beijing Univ Chem Technol (Natural Sci Edition). 2025;52:124–32. (in Chinese).
49. Jin P, Ruan F. Microstructural and Componential characterization of the Plating Technology on Chinese Han Dynasty bronze fragments. *Archaeometry*. 59,274–86 (2016).
50. Liang C, Li W, Yu X, et al. Scientific analysis of the gilt-bronze chariot parasol component of the Eastern Han Dynasty excavated from the Dafenbao cemetery, Pengshan, Sichuan, China. Archaeol Anthropol Sci. 2024;16:158.
51. Ma R, Li Z, Tang M, et al. Microstructural characteristics and formation of the gilded artifacts excavated from Han Tomb situated in Qufu, Shandong, China. npj Herit Sci. 2025;13:93.
52. Zhang J, Liu J, Li J, et al. Scientific Investigations of Lobed Decorated Bronze Yi Gilt with Gold and Silver Unearthed From M10 at Yaotaizi in Jingbeixinqu of Jingzhou. Jianghan Archaeol. 2024;02:133–40. (in Chinese).
53. Liang X. Traditional Chinese gilding technology. Mater Prot. 1990;Z1:83–6. (in Chinese).
54. Yang X. Chinese Fine Gold Craftsmanship and Cultural Relics. *Science Press*. (2008) (in Chinese).
55. Anheuser K. The practice and characterization of historic fire gilding techniques. JOM. 1997;49:58–62.
56. Cai Y, Hu D, Guan L, et al. A study on the Decoration Technology of the Golding and Silvering Bronze of Chariot Pit Wares in Haihunhou. Cult Relics South China. 2019;06:153–60. (in Chinese).
57. Wang H. A Preliminary Scientific Study of Gold Ornaments and Gilded Copper Objects Excavated from Xiao Mausoleum of Emperor Wu. J Natl Museum China. 2023;02:104–10. (in Chinese).
58. Yao Z, Sun S, Zou H, et al. Studies on the Bronzes Excavated from the Tombs in the Xiajiang River Region. Stud History Nat Sci. 2005;02:106–18. (in Chinese).
59. Li W, Li D. Variations of work function and corrosion behaviors of deformed copper surfaces. Appl Surf Sci. 2005;240:388–95.
60. Robin A, Martinez GAS, Suzuki PA. Effect of cold-working process on corrosion behavior of copper. Mater Design. 2012;34:319–24.
61. Yan K, Yao WQ, Cao JL, et al. Electron migration behavior of Au/Cu multilayer films on Si substrates under UV radiation. Phys Chem Chem Phys. 2015;17:5057–62.
62. Jia M, Xu H, Hu P, et al. Microstructures and electrochemical corrosion behaviors of bronze mirror. npj Herit Sci. 2025;13:405.
63. Zhang Y, Zhu C, Yu S. Environmental evolution and human activity over 3000 years in Daning Valley, the Three Gorges of Changjiang River. Sci Geogr Sin. 2001;21:267–71.
64. Li X, Wang G, Sun J, et al. A study on 33 years corrosion behaviour of materials in soil at Three Gorges area. Corros Sci Prot Technol. 1995;01:109. (in Chinese).

65. Oudbashi O, Emami SM, Ahmadi H, et al. Micro-stratigraphical investigation on corrosion layers in ancient bronze artefacts by scanning electron microscopy energy dispersive spectrometry and optical microscopy. Herit Sci. 2013;1:21.
66. Fan X, Wang Q, Wang Y. Non-destructive in situ Raman spectroscopic investigation of corrosion products on the bronze dagger-axes from Yujiaba site in Chongqing, China. Archaeol Anthropol Sci. 2020;12:90.

Figures

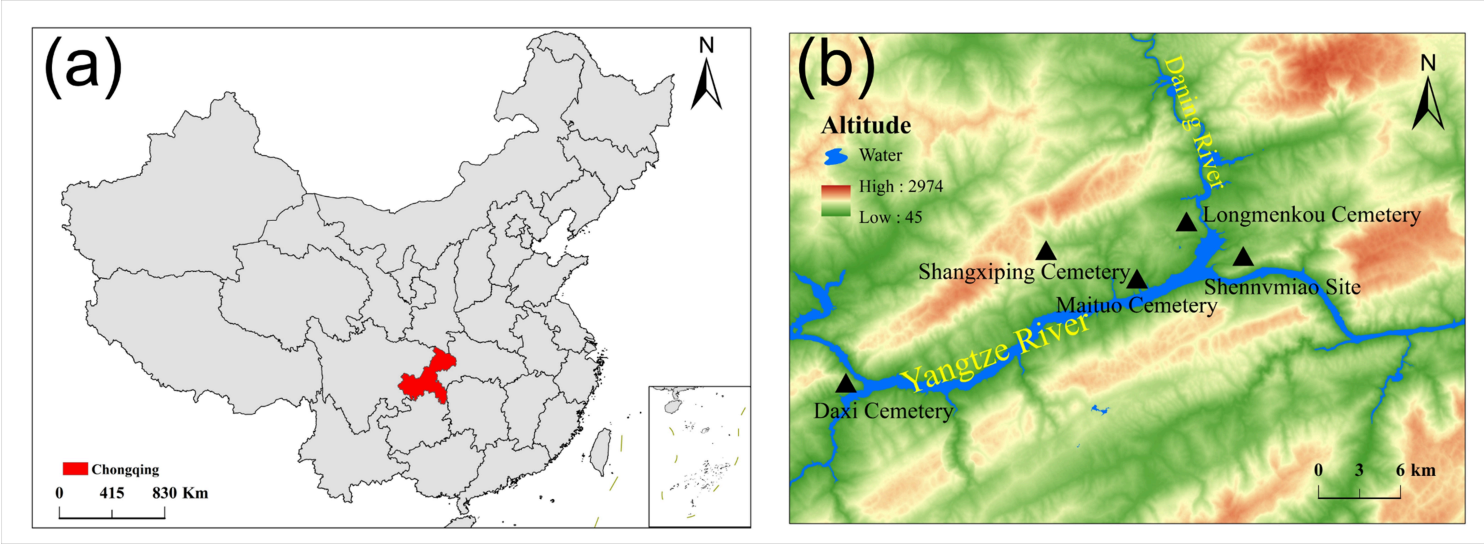


Figure 1

The map of cemetery. a Location of Chongqing municipality in China; **b** Location of archaeological sites in Wushan County.

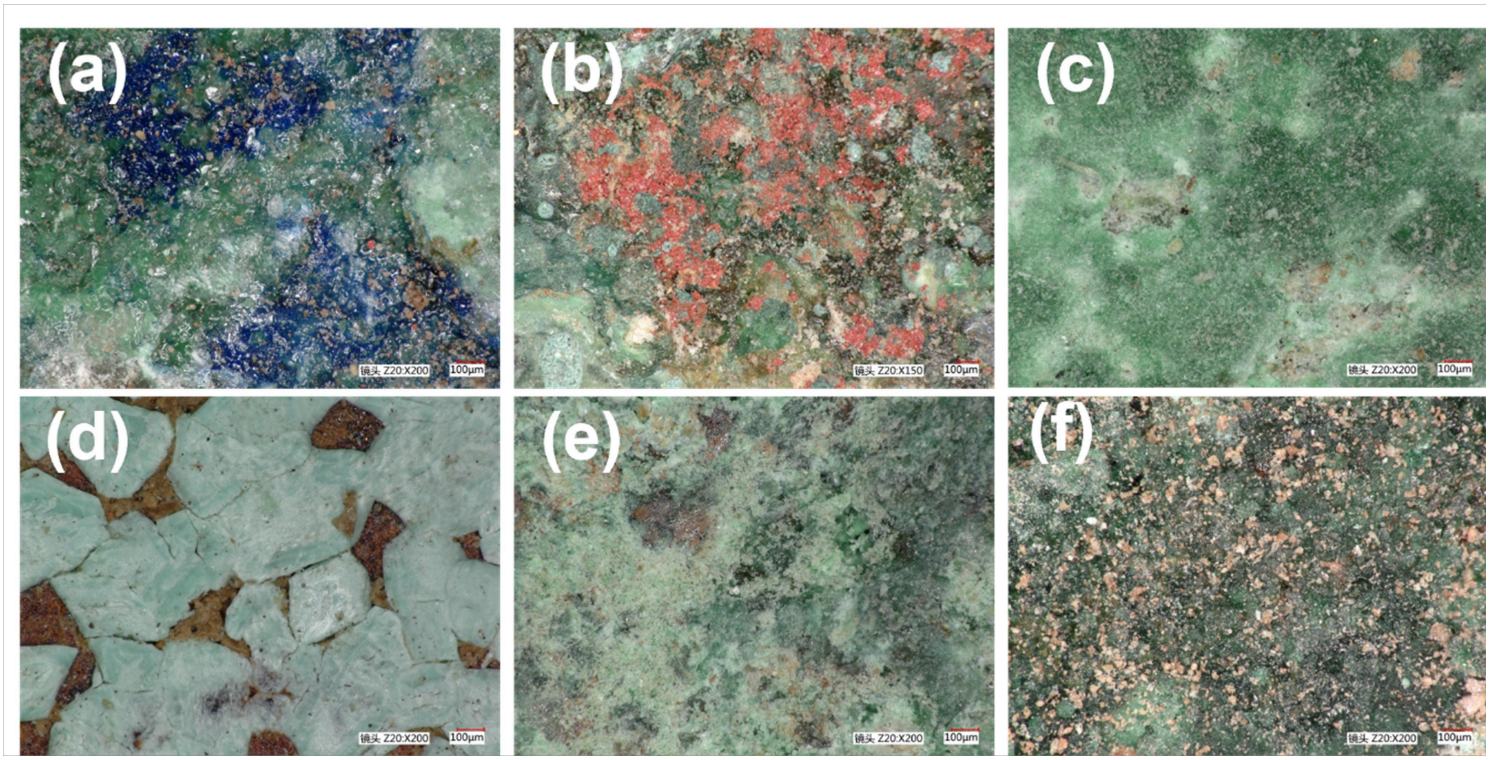


Figure 2

Micrographs of the surfaces. a L1; **b** L2; **c** L3; **d**L4; **e** L5; **f** L6.

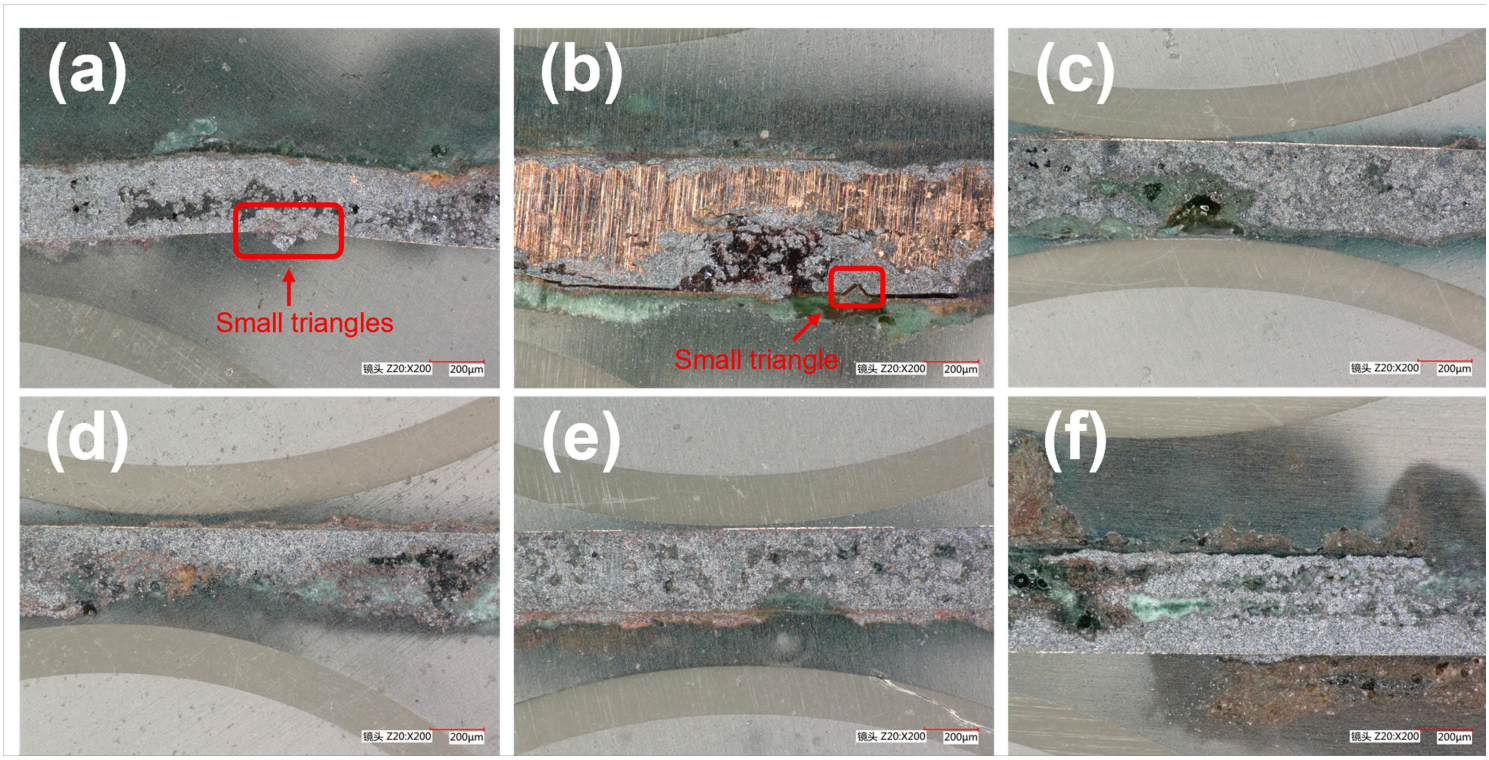


Figure 3

Micrographs of the cross-sections. a L1; **b** L2; **c** L3; **d** L4; **e**L5; **f** L6.

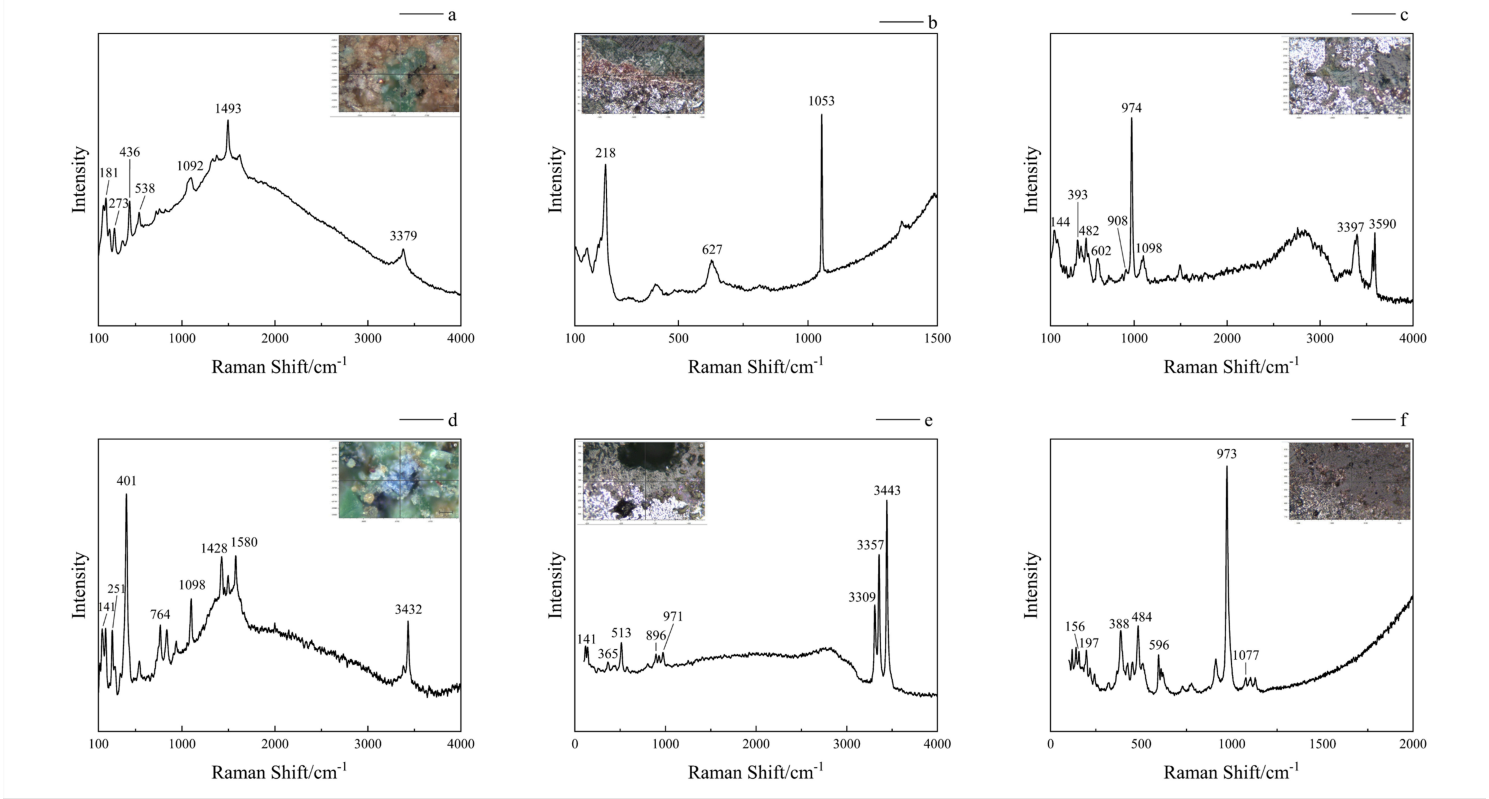


Figure 4

The Raman spectra. a malachite (L1); **b** cuprite, cerussite (L1); **c**brochantite (L5); **d** azurite (L2); **e** atacamite (L3); **f** libethenite (L4).

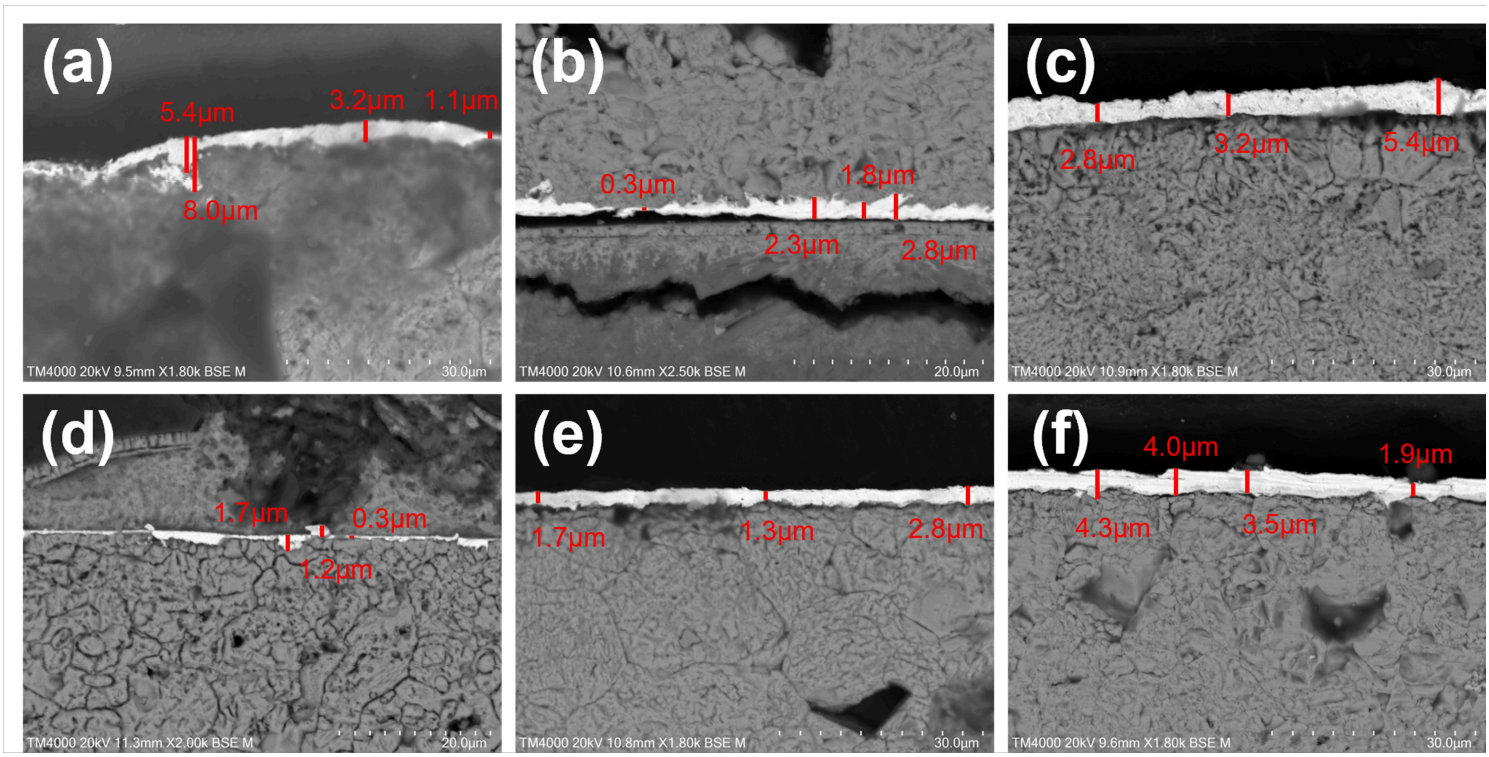


Figure 5

The SEM images of the cross-sections of the gilded layers. a L1; **b** L2; **c** L3; **d** L4; **e** L5; **f**L6.

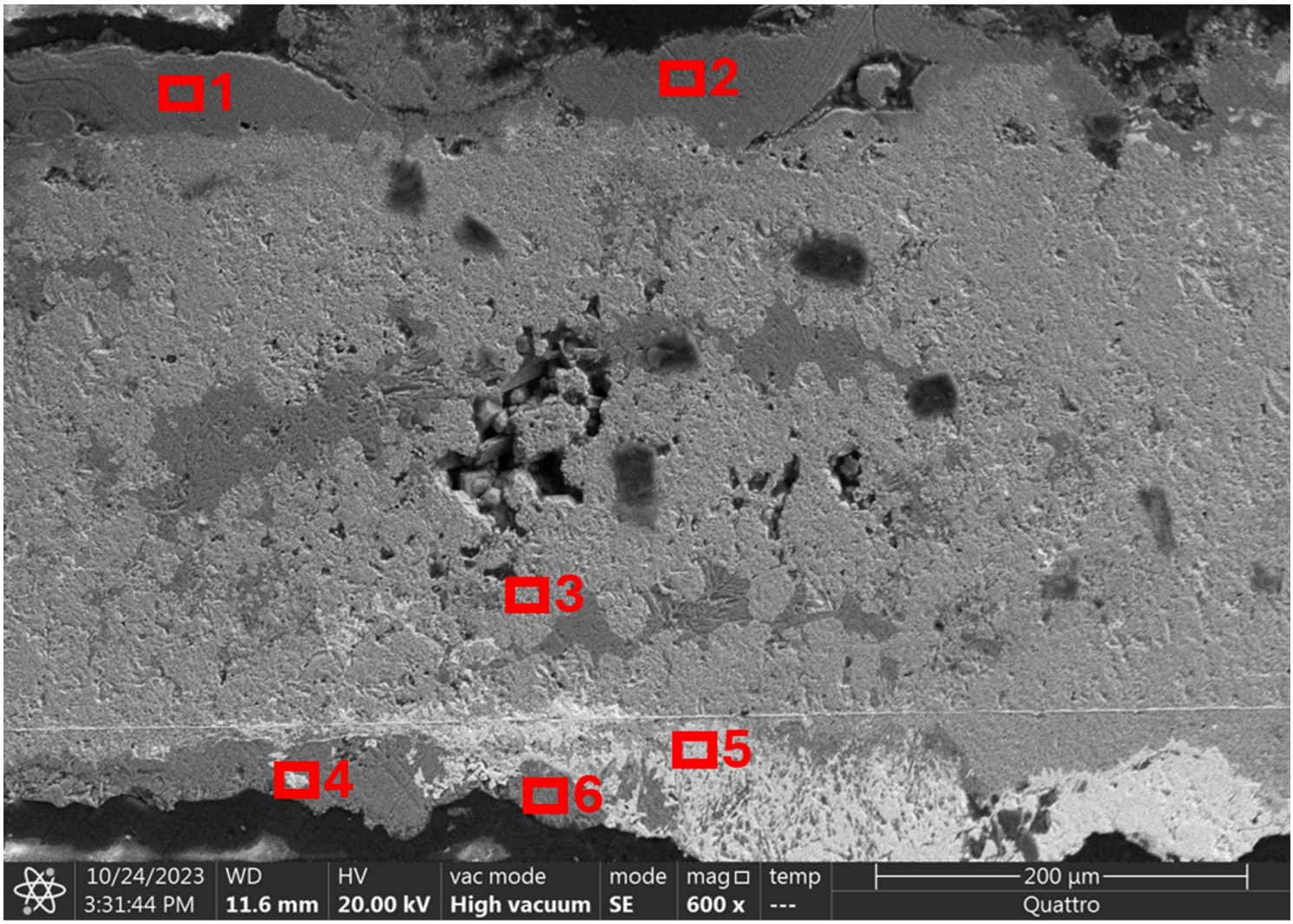


Figure 6

The SEM image of the cross-section of L1.

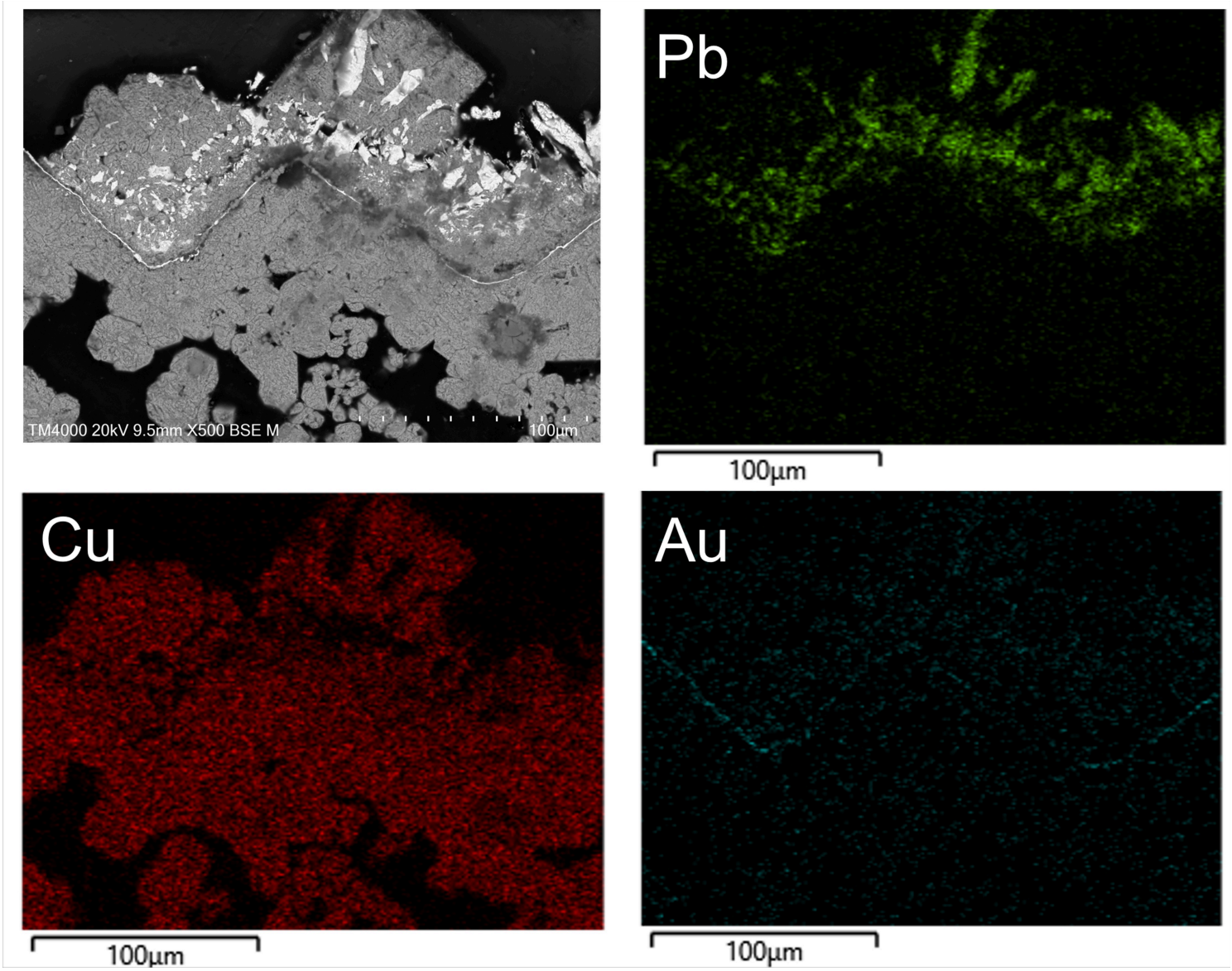


Figure 7

The images of SEM and element mapping of the cross-section of the gilded layers of L1.

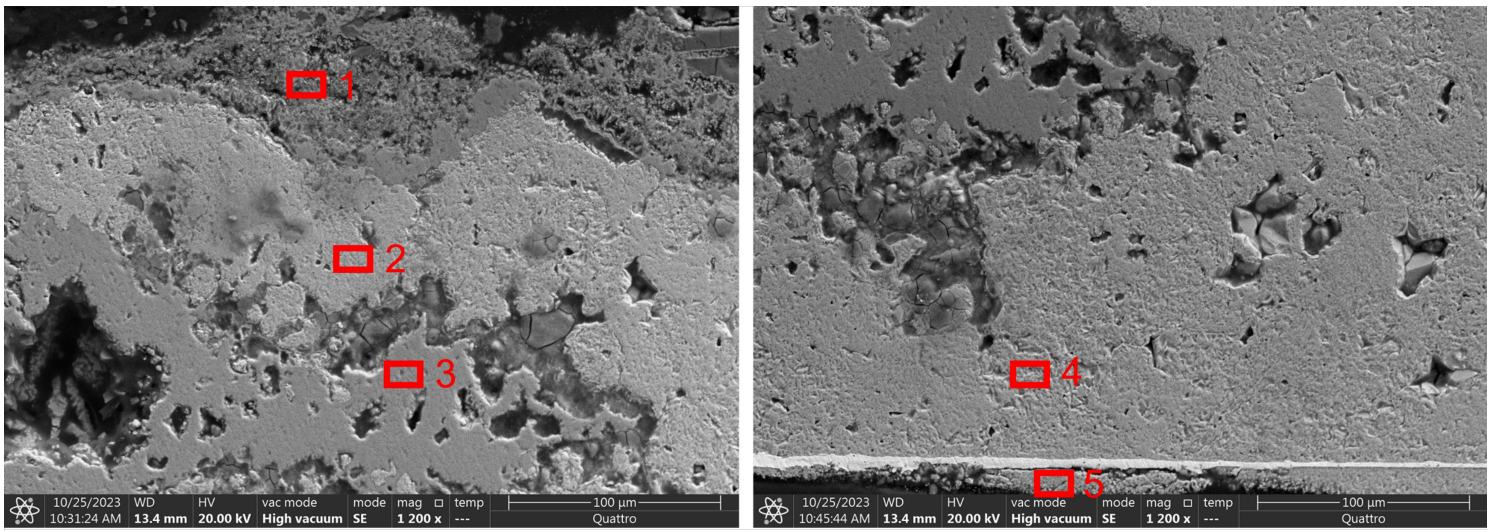


Figure 8

The SEM images of the cross-section of L3.

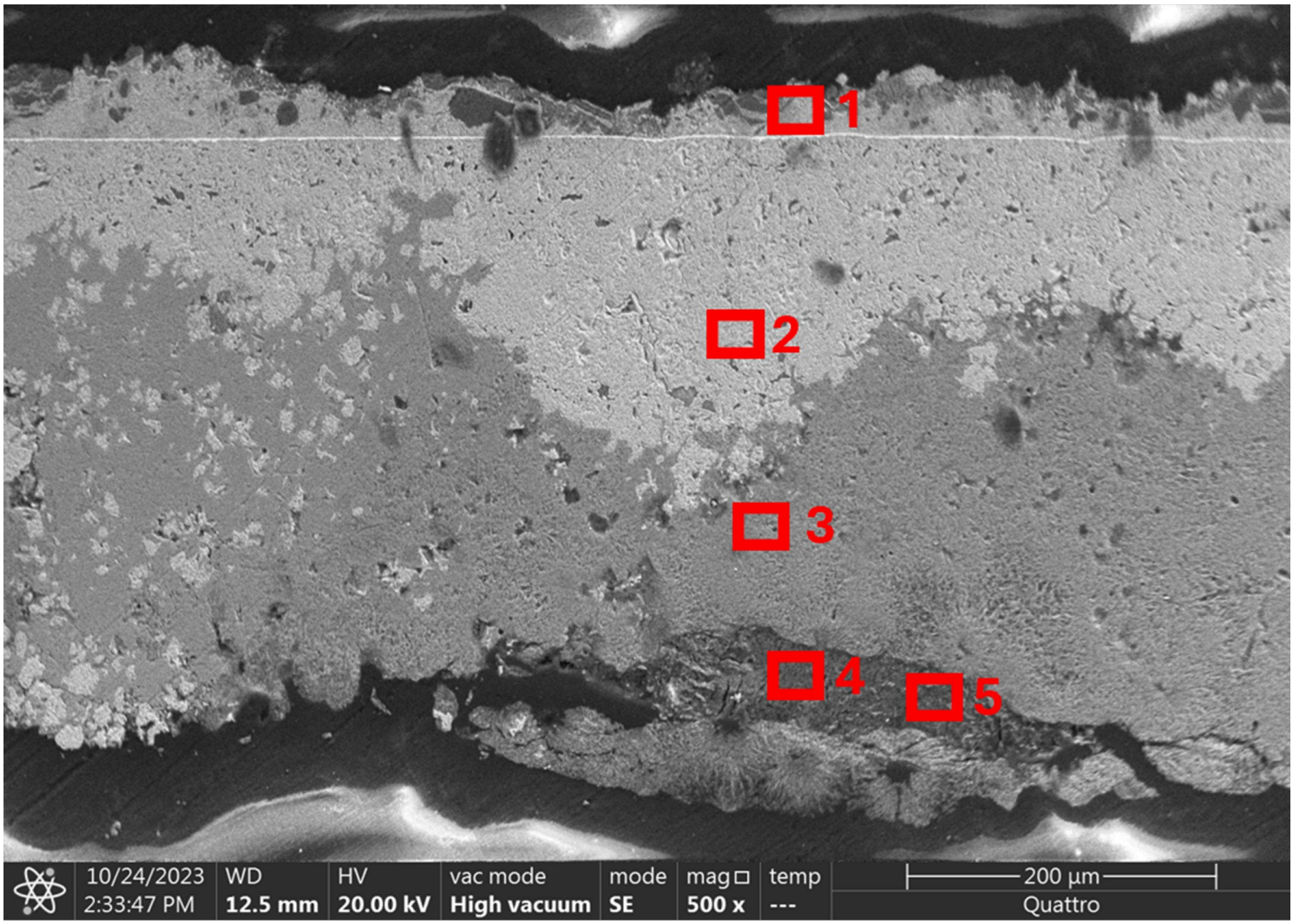


Figure 9

The SEM image of the cross-section of L4.

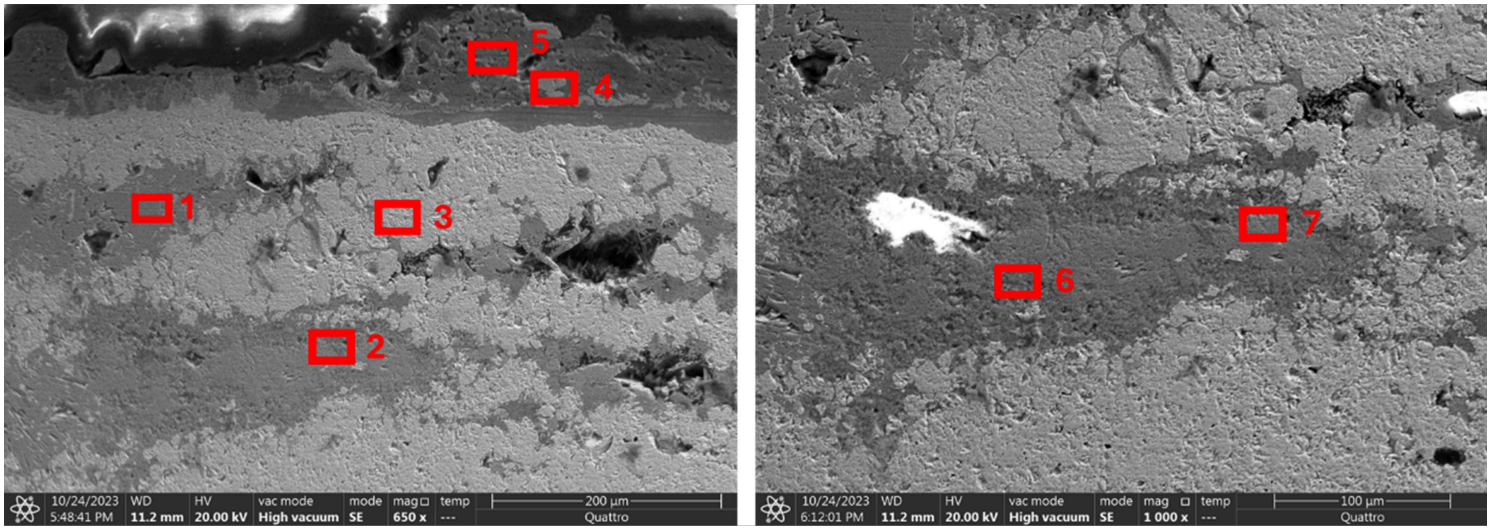


Figure 10

The SEM images of the cross-section of L6.

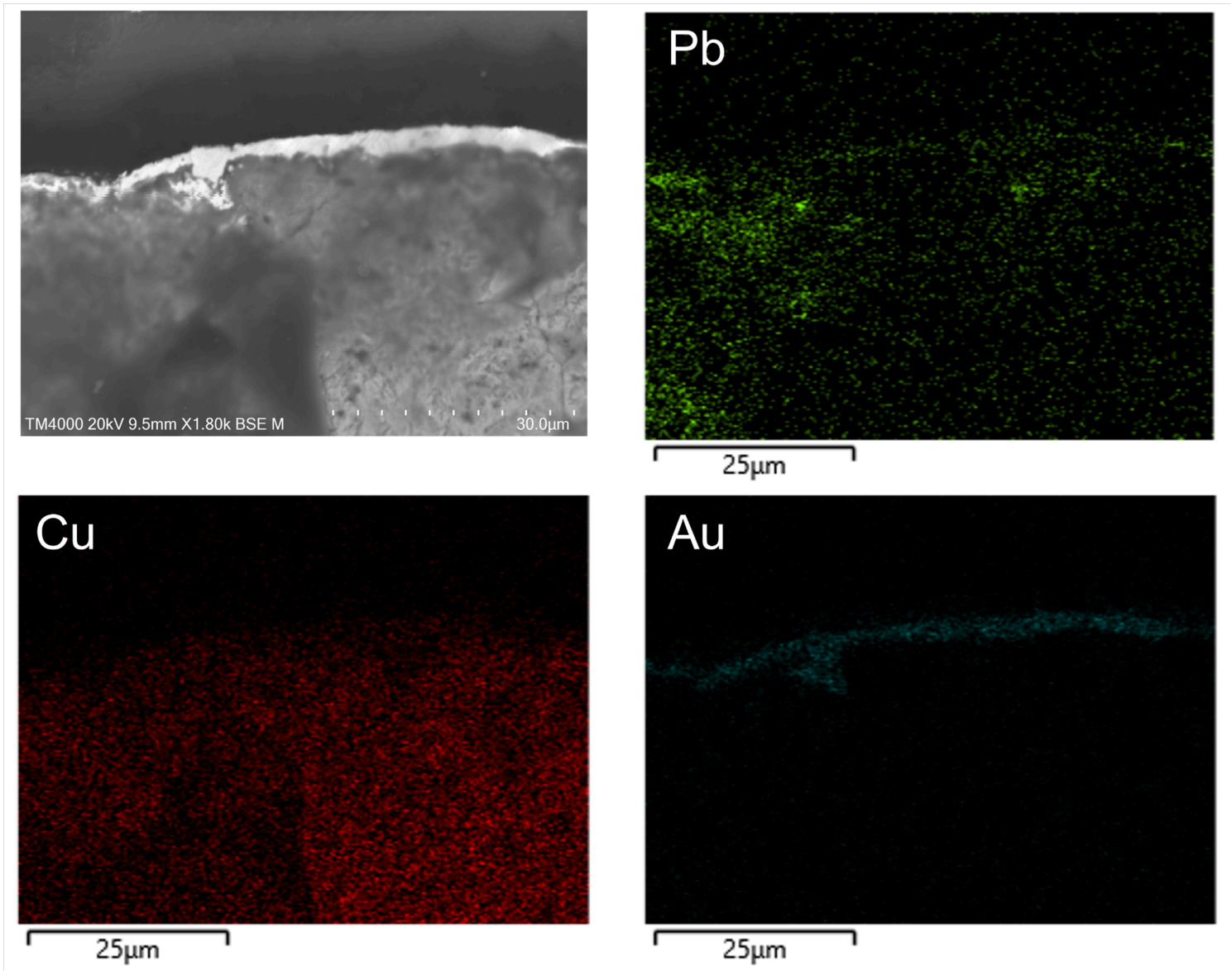


Figure 11

The images of SEM and element mapping of L1